Nano-Micro Lett. (2018) 10:37
https://doi.org/10.1007/s40820-018-0192-6

ARTICLE

Efficient Photoelectrochemical Water Splitting by g-C_3N_4/TiO_2 Nanotube Array Heterostructures

Changhai Liu[1] · **Fang Wang**[1] · **Jin Zhang**[1] · **Ke Wang**[1] · **Yangyang Qiu**[1] · **Qian Liang**[2] · **Zhidong Chen**[2]

Received: 27 November 2017 / Accepted: 15 January 2018 / Published online: 9 February 2018

Highlights

- Well-ordered TiO_2 nanotube arrays (TNTAs) decorated with g-C_3N_4 were fabricated by anodic oxidization of titanium foil and calcination process.
- The g-C_3N_4/TNTA heterojunction efficiently enhanced the photoelectrochemical activity for solar light-driven water splitting. Its photocurrent density and applied bias photon-to-current efficiency were, respectively, ~ 0.86 mA cm^{-2} and ~ 0.25%, about twofold higher compared with those of pristine TiO_2 nanotube arrays.
- The heterojunction expanded the optical absorption range of the TNTAs, accelerated the migration of carriers, and suppressed the recombination of photogenerated electron–hole pairs via an efficient band alignment between TiO_2 and g-C_3N_4.

Abstract Well-ordered TiO_2 nanotube arrays (TNTAs) decorated with graphitic carbon nitride (g-C_3N_4) were fabricated by anodic oxidization and calcination process. First, TNTAs were prepared via the anodic oxidation of Ti foil in glycerol solution containing fluorinion and 20% deionized water. Subsequently, g-C_3N_4 film was hydrothermally grown on TNTAs via the hydrogen-bonded cyanuric acid melamine supramolecular complex. The results showed that g-C_3N_4 was successfully decorated on the TNTAs and the g-C_3N_4/TNTAs served as an efficient and stable photoanode for photoelectrochemical water splitting. The facile deposition method enables the fabrication of efficient and low-cost photoanodes for renewable energy applications.

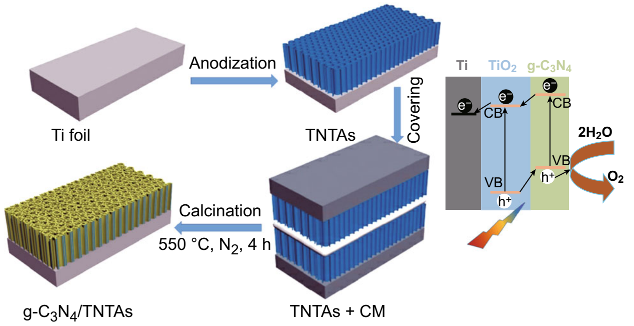

Keywords TiO_2 nanotube arrays · Graphitic carbon nitride (g-C_3N_4) · Heterojunction · Photoelectrochemical · Water splitting

---

Electronic supplementary material The online version of this article (https://doi.org/10.1007/s40820-018-0192-6) contains supplementary material, which is available to authorized users.

✉ Zhidong Chen
zdchen@cczu.edu.cn

[1] School of Materials Science and Engineering, Jiangsu Collaborative Innovation Center of Photovoltaic Science and Engineering, Changzhou University, Changzhou 213164, Jiangsu, People's Republic of China

[2] School of Petrochemical Engineering, Changzhou University, Changzhou 213164, Jiangsu, People's Republic of China

1 Introduction

Photoelectrochemical (PEC) water splitting is a promising process in which solar energy is transformed into chemical energy and stored in the form of hydrogen [1–3]. In the past decades, semiconductor-based photoelectrodes, such as Fe_2O_3 [4, 5], CdS [6, 7], ZnO [8, 9], $CuInS_2$ [10], WO_3 [11], and TiO_2 [12–14], for PEC cells have been extensively utilized to convert solar energy into fuel. TiO_2 nanotube arrays (TNTAs) are commonly employed as photocatalysts owing to their excellent photochemical and chemical stability, non-toxicity, low cost, and well-aligned nanostructures. Furthermore, TNTAs have a higher specific surface area and pore volume compared to TiO_2 nanoparticles for other active catalysts adsorbed onto the surface of both sides of nanotubes [15–17]. Despite the considerable advantages in the morphology of the one-dimensional nanostructure, the photocatalytic activity of pristine TiO_2 is greatly limited by its wide band gap of $\sim$ 3.2 eV, which leads to the extremely low absorption in the visible region of solar spectrum. In addition, the fast recombination rate of the photogenerated electron–hole pairs also restricts their photochemical applications. Therefore, great efforts have been made to expand its absorption range to the visible region, including decoration with precious metals [12, 18], element doping [19, 20], dye-sensitization [21], or coupling with other semiconductors to form a heterojunction [22–24].

Recently, graphite-like carbon nitride (g-C_3N_4), as a significant metal-free polymeric semiconductor with inherent chemical and thermal stability, and a moderate band gap of 2.7 eV, has generated a lot of interest [25–27]. Compared to transition metal oxides and sulfide semiconductor photocatalysts, g-C_3N_4 is composed of strong covalent bonds between carbon and nitride atoms and demonstrates high stability in acidic and alkaline electrolytes, which is favorable for PEC applications [25, 28]. However, owing to the low quantum efficiency and high electron–hole recombination rate [29], the applications of pure g-C_3N_4 are limited by its relatively low photoelectric conversion efficiency. Therefore, there is a significant scope to explore and design novel hybrid materials and improve the applicability of pure g-C_3N_4.

Herein, we fabricated a g-C_3N_4/TNTA heterojunction by combining anodized TNTAs on titanium foil and g-C_3N_4 prepared via the calcination process of the hydrogen-bonded cyanuric acid melamine (CM) supramolecular complex [30]. Owing to the existence of free hydroxyl and amine groups, the CM complex could be attached to TNTAs and amorphous TiO_2. We have presented a facile and simple method to grow carbon nitride on the inner and outer surface of the TNTAs. More importantly, the new heterostructures of g-C_3N_4/TNTAs exhibit enhanced PEC water splitting activity, which is twice that of pristine TNTAs and more than four times that of amorphous TiO_2. In addition, the results of this work proved that the heterojunctions were highly efficient as photoanodes and demonstrated stable performances for PEC water splitting.

2 Experimental Section

2.1 Chemicals

All reagents were of analytical grade and used without further purification. Ammonium fluoride (NH_4F), cyanuric acid, melamine, and glycerol were purchased from Sinopharm Chemical Reagent Co., Ltd.

2.2 Preparation of Photoelectrodes

The preparation of the g-C_3N_4/TNTAs is schematically shown in Fig. 1. In a typical synthetic procedure, Ti foil (99.9%) and a platinum sheet with a size of 1×1 cm^2 were used as the working and counter electrodes, respectively. The electrolyte solution was prepared by dissolving 0.5 wt% of NH_4F in 20 mL H_2O and 80 mL glycerol. The Ti foils (1×4 cm^2 with a thickness of 0.3 mm) were cleaned by ultrasonication in acetone, ethanol, and DI water sequentially. The well-ordered TNTAs on Ti foils were synthesized via a modified one-step anodization procedure at 30 V for 2 h at room temperature. Subsequently, the obtained TNTA precursor was thoroughly rinsed with DI water, annealed at 550 °C in air at a heating rate of 3 °C min^{-1} for 2 h, and naturally cooled to room temperature.

The g-C_3N_4 precursor (CM complexes) was prepared by dissolving cyanuric acid and melamine (1:1) in DI water and stirring for 4 h, after which the white CM complexes were precipitated. The white powders were washed several times with DI water, and the resulting powders were dried at 60 °C in a vacuum oven. The g-C_3N_4/TNTA heterojunctions were prepared by calcining in a tube furnace. A specified amount of CM complexes was placed between two slices of TNTAs (or Ti). These layers were then placed in a ceramic crucible and calcined at 550 °C for 4 h under nitrogen at a heating rate of 3 °C per minute. After heating, the residual powders were blown away by a strong airstream to obtain the g-C_3N_4/TNTAs. In order to investigate the role of the semiconductor, two clean Ti foils without anodic oxidation treatment were used to replace the TNTAs as the substrates. After subjecting to the same calcined process, the g-C_3N_4 thin film was obtained on amorphous TiO_2 and the assembly was used as a photoelectrode for comparison with g-C_3N_4/TNTAs.

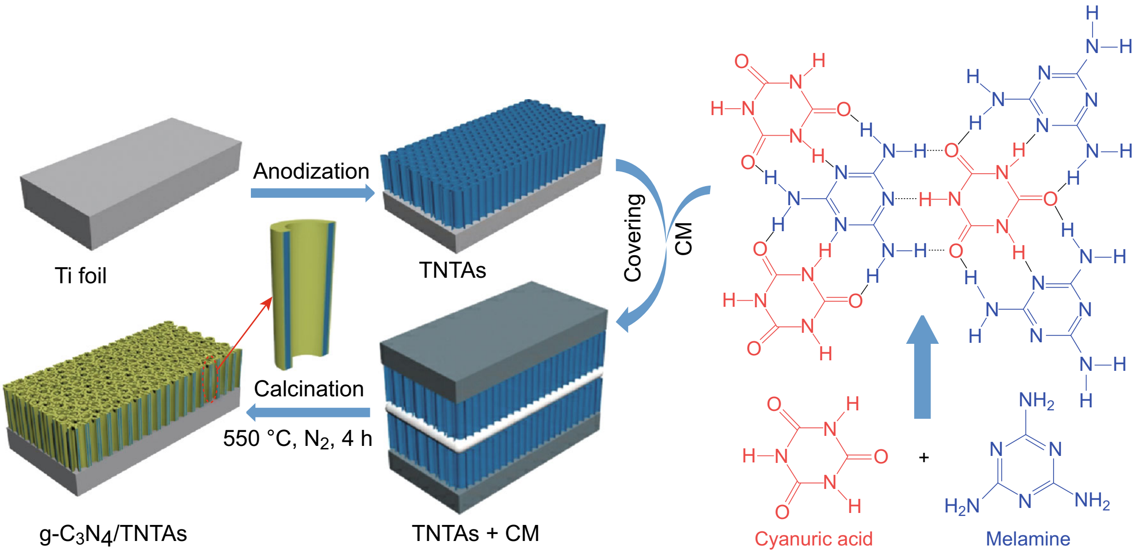

Fig. 1 Schematic diagram of the preparation of TNTAs and g-C_3N_4/TNTA photoelectrodes

2.3 Structural and Optical Characterizations

The crystal structures were determined by X-ray diffraction (XRD) on a PANalytical X'Pert powder diffractometer with Cu K_α radiation ($\lambda = 1.54$ Å). Diffraction angle (2θ) ranged from 10° to 80° and the scanning step was 0.02°. The Raman spectra were obtained on a LabRAM HR Evolution spectrometer (HORIBA Jobin–Yvon) with an excitation wavelength of 532 nm. The morphology of the samples was studied by using a field emission scanning electron microscope (FE-SEM, FEI-quanta 200, 15 kV) and an atomic force microscope (AFM, Digital Instruments Nanoscope III, operating in tapping mode). The microstructure was observed by transmission electron microscopy (TEM) equipped with an energy-dispersive X-ray spectrometer (EDS). The surface compositions and elemental chemical states of the samples were examined by using an X-ray photoelectron spectrometer (XPS) with K-Alpha 1063 (Thermo Fisher Scientific, UK) instrument equipped with an Al Kα monochromator X-ray source. The light absorption of the samples was recorded with a UV–Vis spectrophotometer (UV-2500, Shimadzu, Japan).

2.4 Photoelectrochemical Measurements

The PEC properties of the fabricated samples were measured on an electrochemical workstation (CHI660E) comprised of a three-electrode cell system of an Ag/AgCl reference electrode and a platinum counter electrode in an aqueous solution of 0.1 M Na_2SO_4 as the electrolyte. Light was provided by a 300-W Xe arc lamp and its power density was adjusted to 100 mW cm^{-2}. In our study, all potential readings have been reported with respect to the reversible hydrogen electrode (RHE) using the equation: $E_{\mathrm{RHE}} = E_{\mathrm{Ag/AgCl}} + (0.059 \times 5.6) + 0.197 = E_{\mathrm{Ag/AgCl}} + 0.53$ (V). Linear sweep voltammetry (LSV) curves were collected at a scan rate of 10 mV s^{-1} with or without illumination. The periodically illuminated LSV measurement with on–off light was also recorded. In addition, the electrochemical impedance spectra (EIS) of the different photoelectrodes were obtained in the frequency range of 100 kHz–0.1 Hz without applied bias. The Mott–Schottky plots were obtained at 10 kHz frequency. The transient open-circuit potentials (OCPs) were also measured in the dark and under light illumination.

3 Results and Discussion

XRD studies were performed to investigate the phase purity and crystallographic structure of the as-prepared g-C_3N_4/TNTAs photoanode. As demonstrated in Fig. 2a, the TNTAs belong to the pure anatase phase (JCPDS card No. 21-1272) [31], and their crystal structure was almost unchanged after the loading of g-C_3N_4. The diffraction peaks at ~ 25° and ~ 37.8° of the TNTAs and the g-C_3N_4/TNTAs heterojunction were assigned to the TiO_2 (101) and (004) peaks, respectively. Meanwhile, the peak at ~ 27.3° was attributed to the interlayer stacking of aromatic systems (002) of g-C_3N_4 (JCPDS card No. 87-1526) [32]. It is worth noting that the intensity of the (004) peak of g-C_3N_4/TNTAs was significantly reduced as compared with that of pure TNTAs, confirming the loading of g-C_3N_4 layers on the TNTA surface. The crystalline formation in the TNTAs and the loading of g-C_3N_4 was also confirmed by Raman scattering (Fig. 2b). Compared to

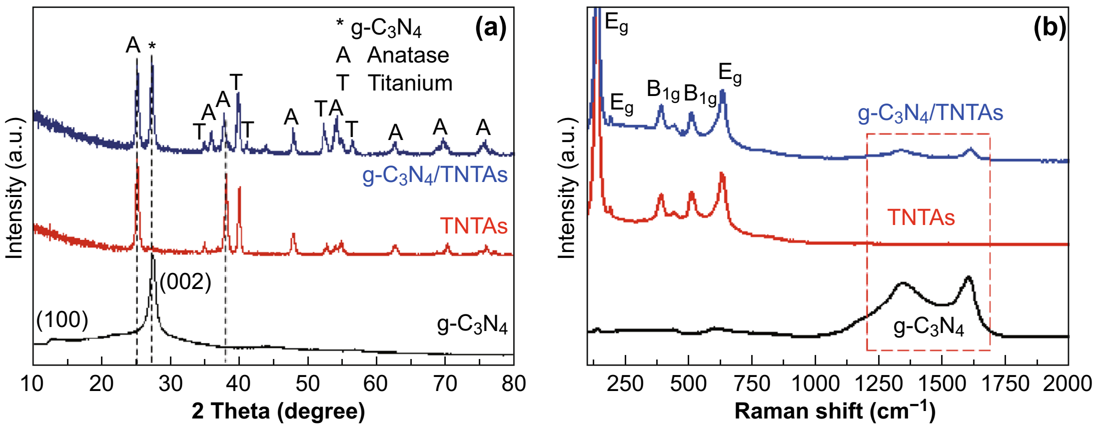

Fig. 2 **a** XRD and **b** Raman spectra of g-C_3N_4, TNTAs, and g-C_3N_4/TNTAs

pristine TNTAs, the specific peaks of the g-C_3N_4/TNTAs at 1337 and 1617 cm^{-1} were attributed to the symmetric E_{2g} vibration mode in the graphite-like structure and disordered sp^2 micro-domains introduced by linking with N atoms [33–35], which indicated the successful loading of the graphitic C_3N_4 layer on the TNTAs. In addition, the annealed TNTAs and g-C_3N_4/TNTAs exhibited a series peaks at 146, 197, 395, 514, and 639 cm^{-1}, which were characteristic of anatase TiO_2 [36]. The Raman bands at 146, 197, and 639 cm^{-1} corresponded to the E_g mode, and two other peaks at 395 and 514 cm^{-1} were assigned to the B_{1g} mode. The Raman band observed at 144 cm^{-1} in the rutile phase of TiO_2 is sharp but of weak intensity, which is significantly different from the intense and sharp band observed in the case of anatase [37].

Figure 3a, b is the SEM images of the TNTAs and g-C_3N_4/TNTA layers grown on the Ti substrate, respectively. Under the optimized electrochemical anodization conditions (as described in the Experimental section), the average diameter of the TNTAs was ~ 150 nm, as shown in Fig. 3a. Subsequently, the tube layers were decorated with g-C_3N_4 via calcination of the CM powder under a nitrogen atmosphere. In order to compare the different roles of the tubes, titanium foil was also used as a substrate to decorate g-C_3N_4 under the same conditions (labeled as g-C_3N_4/TiO_2). The SEM image in Fig. 3b clearly shows that after the g-C_3N_4 decoration process, the tube diameter decreased to only ~ 100 nm, indicating that the g-C_3N_4 was successfully decorated on the inner and outer walls of the tubes, leading to a decrease in the inner diameter of tubes. As described in Fig. S1, a continuous and compact g-C_3N_4 film was formed on the amorphous TiO_2 surface. The TEM image of the g-C_3N_4/TNTAs given in Fig. 3c illustrates their distinct tubular structure; the tubes possessed a uniform diameter of ~ 100 nm. The EDS spectrum of g-C_3N_4/TNTAs (Fig. 3d) showed the peaks characteristic of the Ti, O, and C elements, further confirming the decoration of g-C_3N_4 on TiO_2. Curiously, the nitrogen peak was not observed in the EDX spectrum. This was attributed to the low loading of g-C_3N_4 on the surface of the TNTAs and the low content of nitrogen in the sample. The existence of nitrogen was instead confirmed by XPS. Figure 3e shows the high-angle annular dark field (HAADF) scanning transmission electron microscopy (STEM) images of the g-C_3N_4/TNTAs heterojunctions. The EDS mapping analysis shows the uniform distribution of each element at the inner or outer surface of the TNTAs (Fig. 3f–i), indicating the successful coating of g-C_3N_4 during the high-temperature annealing process from the CM precursor.

In order to characterize the changes in the tube diameter more intuitively, we prepared a statistical histogram of the number of nanotubes with different r_{in}/r_{out} values for TNTAs and g-C_3N_4/TNTAs, where r_{in} and r_{out} refer to the inner and outer diameters of the nanotubes, respectively (Fig. 4). The value of r_{in}/r_{out} was used to evaluate the thickness of the g-C_3N_4 layers, i.e., a smaller value represented a larger thickness of the g-C_3N_4 layers on the surface of the TNTAs and vice versa. As shown in Fig. 4, the average value of r_{in}/r_{out} for g-C_3N_4/TNTAs was ~ 40%, which was much smaller than that of pristine TNTAs and implied that g-C_3N_4 was effectively decorated on the inner and outer walls of the tubes via calcination of the CM complex.

The surface morphology of the nanotube arrays was further investigated by AFM, as shown in Fig. 5. The characteristic two-dimensional (2D) images of the TNTAs and g-C_3N_4/TNTAs are shown in Fig. 5a, c, respectively. The as-prepared TNTAs with well-defined tubes can be observed, and it is also evident that the inner diameters of these tubes were greatly decreased upon coating with g-C_3N_4. A close inspection of the 2D AFM images revealed that the tube wall thicknesses of TNTAs and g-C_3N_4/TNTAs were ~ 59 and 91 nm, respectively.

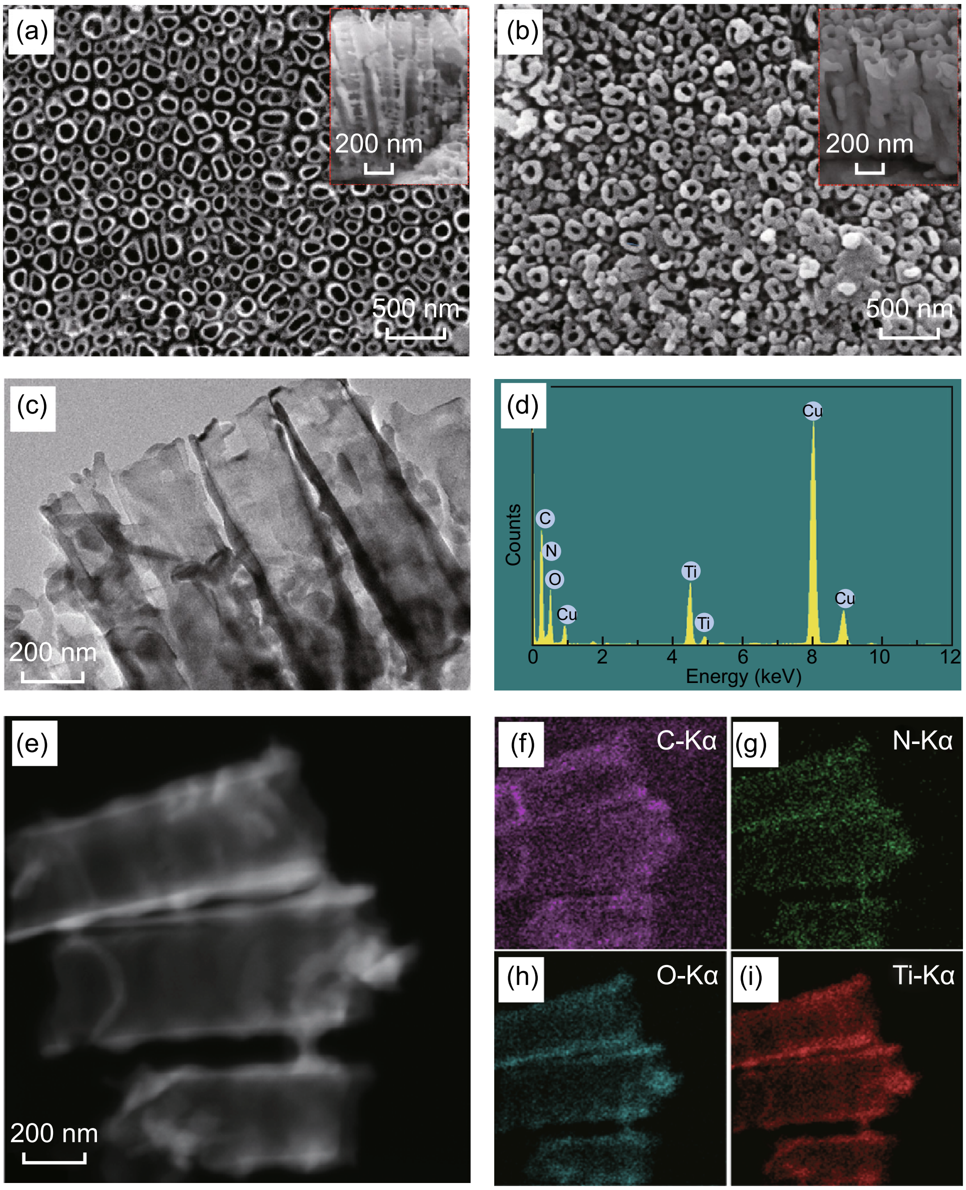

Fig. 3 SEM images of the as-synthesized **a** TNTAs and **b** g-C_3N_4/TNTAs. **c** TEM image and **d** EDX spectrum of g-C_3N_4/TNTAs. **e**, **f** Elemental mapping results of g-C_3N_4/TNTAs

XPS was employed to probe the surface chemical compositions and valence states of g-C_3N_4/TNTAs. Figure 6a presents the overall XP spectrum of the heterojunction, which indicated the presence of Ti, O, C, and a small amount of N from the g-C_3N_4. Figure 6b shows the high-resolution XP spectrum of the Ti 2p state in the g-C_3N_4/TNTAs, with the two different peaks of Ti $2p^{1/2}$ and Ti $2p^{3/2}$ and their binding energies (BE) of 458.9 and 464.6 eV, respectively, which were derived from Ti^{4+} in TiO_2, according to the results of XRD and Raman spectroscopy. It is worth noting that the BE of Ti 2*p* in g-C_3N_4/TNTAs was slightly positively shifted as compared with that of pristine TNTAs, indicating the presence of interactions between the g-C_3N_4 and TNTAs in the form of charge transfer from the electron-rich g-C_3N_4 surface to the unoccupied orbital of Ti^{4+} in TiO_2. The high-resolution C 1s XP spectrum, as shown in Fig. 6c, can be deconvoluted into three peaks at 284.9, 286.6, and 288.6 eV, indicating that carbon possesses three diverse chemical states. The peak at 284.9 eV corresponded to the signal of graphite-like sp^2-hybridized C–C, ascribed to the carbon species adsorbed on the surface of g-C_3N_4. The peaks at 286.6 and 288.6 eV corresponded to C–OH and C–N=C bonds of the heterocycle rings, respectively [38, 39]. Figure 6d shows the XP spectrum of N 1s, which was deconvoluted into three peaks at 399.4, 400.6, and 402.3 eV. The peak at

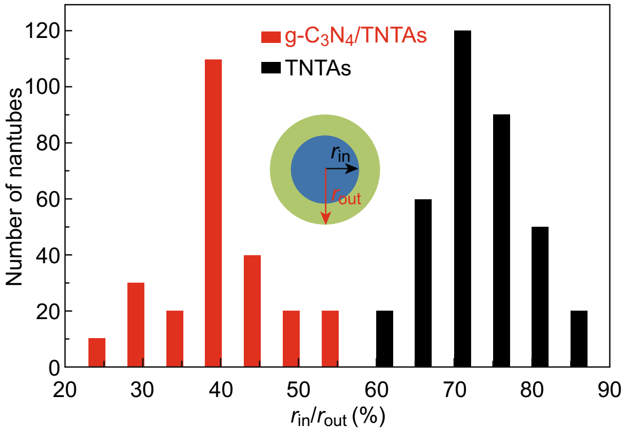

Fig. 4 Number of nanotubes with different r_{in}/r_{out} values for TNTAs (black) and g-C_3N_4/TNTAs (red). (Color figure online)

399.4 eV was typical of the sp^2-hybridized nitrogen (C–N=C), and the peaks at 400.6 and 402.3 eV corresponded to tertiary nitrogen N–$(C)_3$ groups linking the structural motif and amino groups with a hydrogen atom ($(C)_2$–N–H) in connection with structural defects and incomplete condensation [40–42].

To further understand the electronic band structures and photocatalytic properties, the UV–Vis diffuse reflectance spectra (DRS) were obtained to characterize the TNTAs and g-C_3N_4/TNTAs. Figure S2a shows the UV–Vis absorption spectra converted from the reflection absorbance spectra by the standard Kubelka–Munk method. The pristine TNTAs and g-C_3N_4/TNTAs exhibited an absorption edge at ~ 400 nm, and the light absorption of g-C_3N_4/TNTAs was greatly enhanced [43]. In order to calculate the band gaps, the corresponding $(\alpha h\upsilon)^{1/2}$ were plotted versus the photon energy ($h\upsilon$) [44], as shown in Fig. S2b. The band gaps of the TNTAs and g-C_3N_4/TNTAs were calculated to be 3.23 and 3.10 eV, respectively, by extrapolating their plots to $(\alpha h\upsilon)^{1/2} = 0$, according to the linear-fit lines. To determine the existence of g-C_3N_4 in the photoanode heterostructure, the FTIR spectrum was obtained. As shown in Fig. S3, the FTIR spectrum of pristine g-C_3N_4 was very similar to that of g-C_3N_4, consistent with previous reports [45]. The absorption peaks located at 1230, 1316,

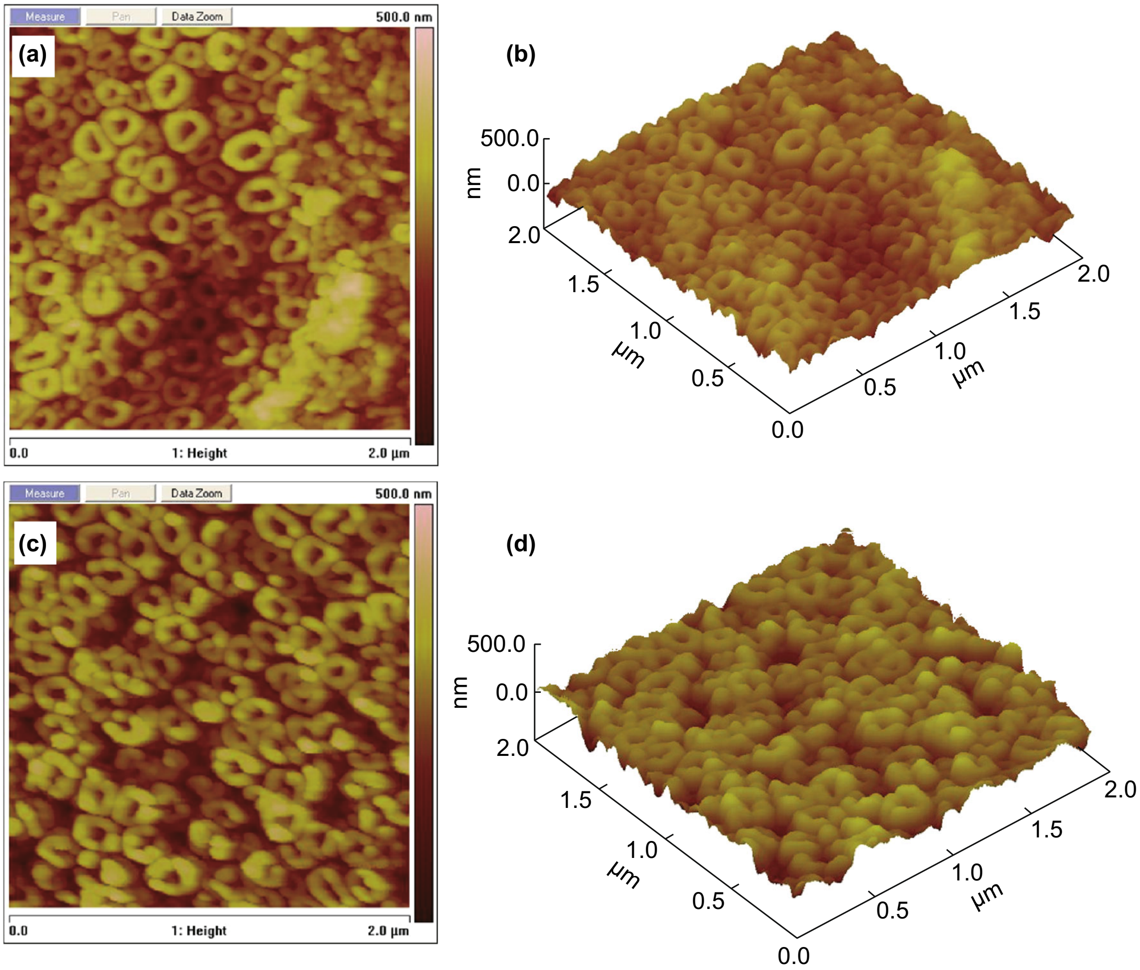

Fig. 5 Top view and 3D AFM images (2 × 2 μm^2) of **a**, **b** TNTAs and **c**, **d** g-C_3N_4/TNTAs

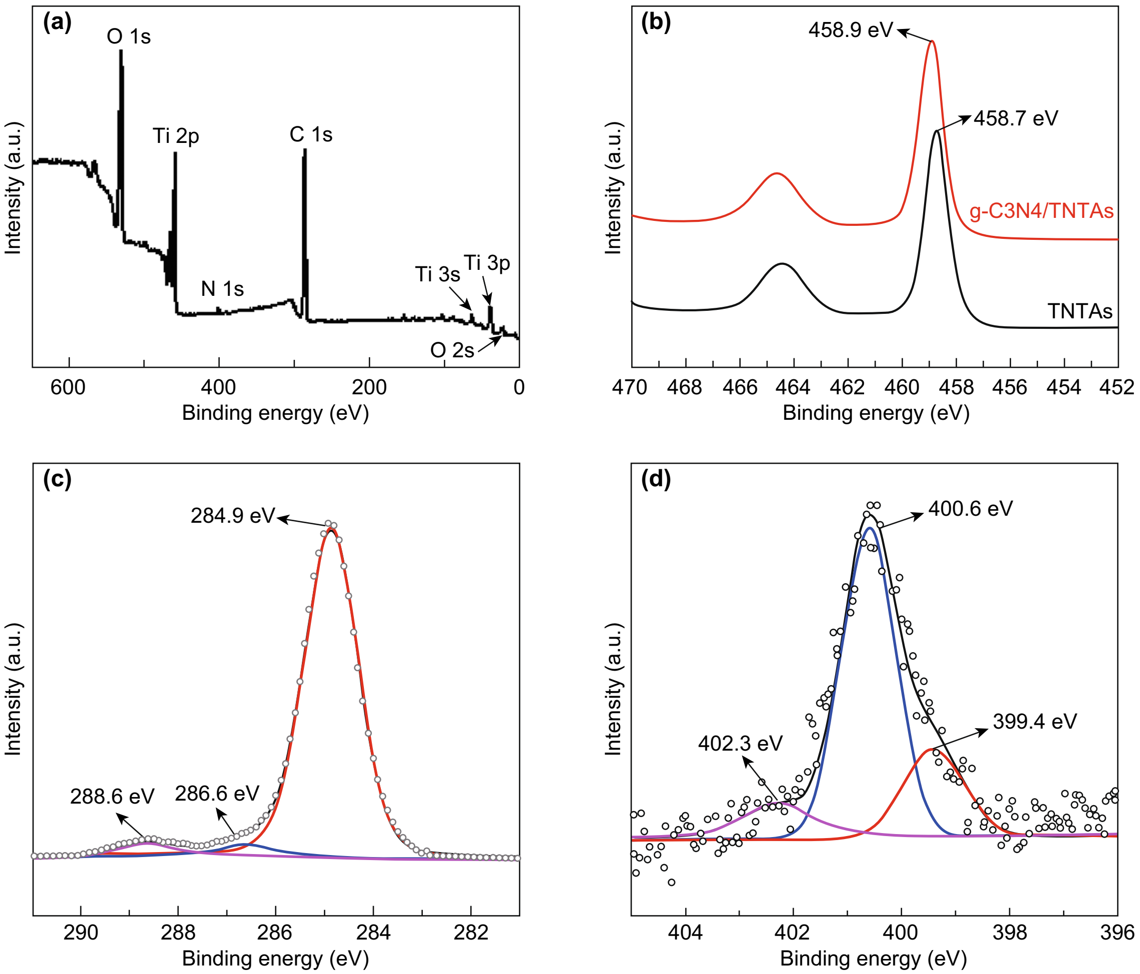

Fig. 6 XPS spectra of g-C_3N_4/TNTAs: **a** survey scan, **b** Ti 2p, **c** C 1s, and **d** N 1s scans

1398, 1553, and 1631 cm^{-1} were related to the typical stretching modes of aromatic C–N [46]. The wide peak observed at wavelengths higher than 3000 cm^{-1} is usually attributed to the H_2O molecules adsorbed on the surface of the materials. The absorption peak at 808 cm^{-1} was typical of the out-of-plane bending mode of the thiazine unit. Compared to the IR spectrum of pristine g-C_3N_4, a series of similar peaks were observed in the case of g-C_3N_4/TNTAs, which indicated a full coverage of g-C_3N_4 over the TNTAs.

Compared to the pristine TNTAs, the combination of TNTAs and g-C_3N_4 exhibits attractive features for enhanced PEC performance. A series of LSV measurements were carried out on the electrochemical workstation CHI660E. Typical plots of photocurrent density vs. bias potential in the potential window of − 0.4 to + 1.3 V versus Ag/AgCl with 0.1 M Na_2SO_4 (pH 6.8) as electrolyte are shown in Fig. 7a. The photocurrent density of the g-C_3N_4/TNTA photoanode at a potential of 0.7 V versus Ag/AgCl (i.e., 1.23 V vs. RHE) was ~ 0.86 mA cm^{-2}, which was almost twice that of pristine TNTAs. Furthermore, the photocurrent densities of g-C_3N_4/TiO_2 and amorphous TiO_2 were determined to be 0.19 and 0.07 mA cm^{-2}, respectively, which were obviously lower than that of the corresponding g-C_3N_4/TNTA and TNTA photoanodes. This suggested that the crystalline TiO_2 nanotubes had a more distinct photoresponse in comparison with the amorphous TiO_2 film. Figure 7b displays the transient photocurrent density (*I*–*t*) of the g-C_3N_4/TNTA and TNTA photoanodes under interrupted illumination at a potential of 0.7 V versus Ag/AgCl. With the on/off switching of light, there was a sharp increase and decrease in the photocurrent density, illustrating a quick photoresponse of the photoanodes. The photocurrents of the different photoanodes were almost of the same order of magnitude. The linear sweep voltammetry results are shown in Fig. 7a. The photocurrent density of pure g-C_3N_4 decorated on the surface of fluorine-doped tin oxide (FTO) glass was also tested (Fig. S4) and found to be a low value of 0.35 μA cm^{-2}. This low value indicated the poor photoresponse of pure g-C_3N_4. Therefore, the enhanced photocurrent density of g-C_3N_4/TNTAs could be attributed to

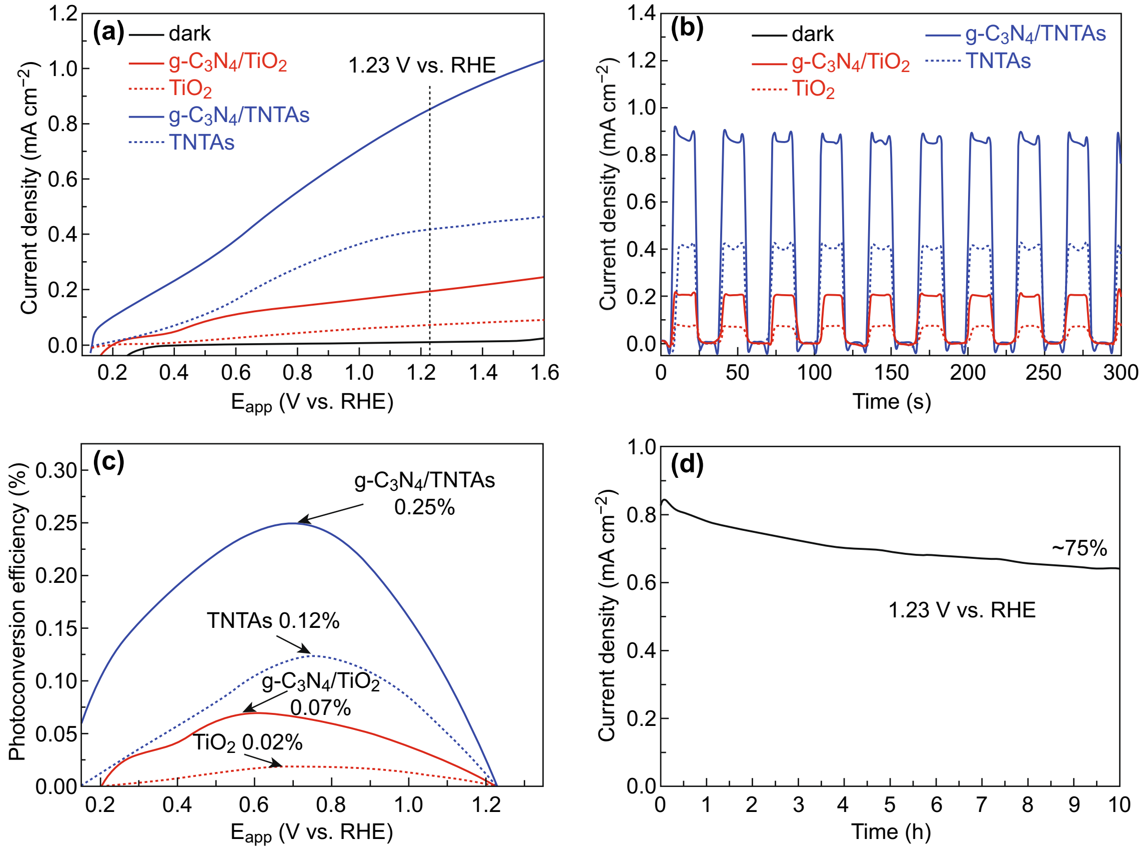

Fig. 7 **a** Current–potential curves of the g-C_3N_4/TNTA photoanode and reference samples (TNTAs, amorphous TiO_2, and g-C_3N_4/TiO_2) under light irradiation (100 mW cm^{-2}). The dark line indicates the dark current density. **b** Time-dependent photocurrent density of different photoanodes under intermittent light irradiation. **c** Photoconversion efficiency as a function of applied potential for different photoanodes. **d** Chronoamperometry plot (*I*–*t*) of the g-C_3N_4/TNTAs measured in 0.1 M Na_2SO_4 with a three-electrode system at 1.23 V_{RHE} for 10 h

the synergistic effect of the heterojunction between TNTAs and g-C_3N_4.

The applied bias photon-to-current efficiencies (ABPE) of the photoanodes for PEC water splitting were estimated according to the following equation [47]:

$$\mathrm{ABPE}\ (\%) = \left(\frac{I \times (1.23 - V_{\mathrm{app}})}{P_{\mathrm{incident}}}\right) \times 100\% \quad (1)$$

where V_{app} is the applied external potential vs. RHE, I is the measured current density, and P_{incident} is the power density of the incident light. The calculated ABPE of the different photoanodes are illustrated in Fig. 7c. The maximum efficiency of the g-C_3N_4/TNTA electrode was ∼ 0.25% (at 0.70 V vs. RHE), i.e., ∼ 2.08 times higher than that of pristine TNTAs (0.12% at 0.76 V vs. RHE). However, the ABPE of g-C_3N_4/TiO_2 and amorphous TiO_2 were 0.07% (at 0.59 V vs. RHE) and 0.02% (at 0.72 V vs. RHE), respectively. The improved ABPE of g-C_3N_4/TNTAs were attributed to the creation of the heterojunction of the TiO_2 nanotubes and g-C_3N_4, which could accelerate the charge migration and promote carrier separation. Furthermore, the g-C_3N_4/TNTAs demonstrated excellent stability (Fig. 7d), as the photocurrent remained relatively stable and retained ∼ 94% of its initial value after more than 14,000 s of continuous testing under light irradiation at 1.23 V versus RHE. The outstanding PEC performance was attributed to the optimal g-C_3N_4/TNTAs heterojunction structure, in which the graphene-like structure of g-C_3N_4 enhanced photoabsorption and simultaneously accelerated the charge separation between TiO_2 nanotubes and g-C_3N_4 [48].

The EIS data are an important tool obtained from the Nyquist plots to further evaluate the kinetics of charge transfer at the electrode/electrolyte interface under both dark and light irradiation conditions. The EIS Nyquist plots (Fig. 8) can be developed by the ZsimpWin software using the R((RQ)(RQ)) circuit model, including solution resistance (*R*), charge transfer resistance (R_3) as the main research object, electrode resistance (R_2), and electrochemical double-layer capacitance (*Q*). The fitting curve (full line) was well-matched with the experimental curve (dotted line), demonstrating a valid circuit model. It was evident that the radii for these three electrodes were significantly larger in the dark than those under light

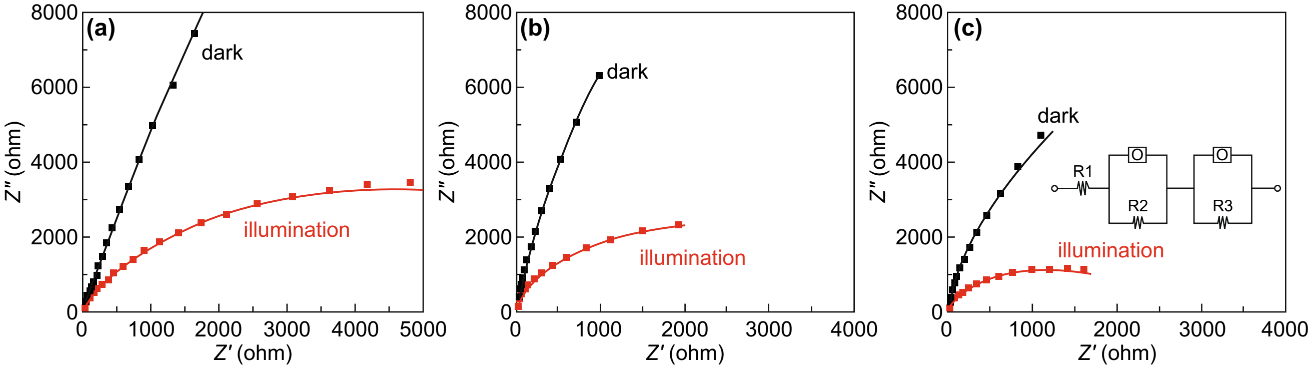

Fig. 8 Nyquist plots of **a** g-C_3N_4/TiO_2, **b** TNTAs, and **c** g-C_3N_4/TNTAs electrodes in dark and with light irradiation

illumination, indicating a larger resistance in the former case that allowed only a few charge transmissions. Upon light irradiation, the electrode radii were noticeably reduced, among which g-C_3N_4/TNTAs demonstrated the largest decrease (Fig. 8c). This change indicated that the electron–hole pair separation rates and carrier migration rates were greatly enhanced in the heterojunction [49]. The specific fit values of circuit components are listed in Table 1. Under light, the R_3 values for all samples were significantly reduced as compared to the resistances under darkness, among which g-C_3N_4/TNTAs demonstrated the largest decrease from 2.929×10^4 to 2.482×10^3 Ω. The significantly improved charge separation and migration potential may be responsible for the enhanced PEC performance, which is in complete agreement with the results of LSV and EIS.

In order to explore the injection direction of photogenerated electrons, OCP transient tests of the prepared electrodes were carried out. The results of these experiments are shown in Fig. 9. All of the electrodes showed a negative increase in voltage under light irradiation, suggesting that the photogenerated electrons are injected from the semiconductor film into the Ti foil substrate [50, 51], generating the anodic photocurrent in *I–V* and *I–t* measurements. It can be inferred that the prepared films act as n-type semiconductor materials, according to the formation mechanism of anodic and cathodic photocurrent in the PEC tests. The difference between the voltages in the dark and under light illumination is the generated voltage. It is worth noting that the g-C_3N_4/TNTA electrode showed the largest generated photovoltage (0.260 V) among the three electrodes, which also implied its remarkable photoelectric conversion ability.

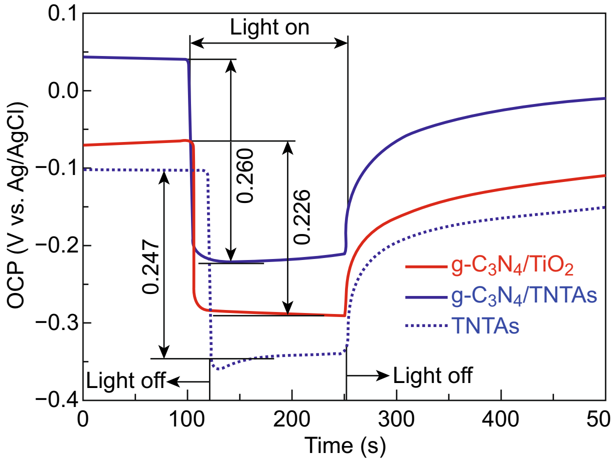

Fig. 9 Transient OCPs of g-C_3N_4/TNTAs, TNTAs, and g-C_3N_4/TiO_2 photoanodes

To investigate the charge transport behavior, Mott–Schottky (MS) measurements were performed, as shown in Fig. 10a, b, with linear segments representing the depleted states of the majority carriers in the space charge region. Both samples showed positive slopes, which implied that TNTAs and g-C_3N_4/TNTAs are n-type semiconductors [52]. According to the MS equation [53], the g-C_3N_4/TNTAs in Fig. 10b showed a much smaller slope than that

Table 1 *Z*-fit equivalent circuit data of g-C_3N_4/TiO_2, TNTAs, and g-C_3N_4/TNTA electrodes

	R(Ω)	Q ($\times 10^{-5}$ F)	n	R_2 (Ω)	Q ($\times 10^{-4}$ F)	n	R_3 (Ω)
g-C_3N_4/TiO_2 (dark)	16.29	7273	0.6432	7.59	5.829	0.8858	235,500
g-C_3N_4/TiO_2 (light)	17.14	4.492	1	1.649	1.156	0.8073	8928
TNTAs (dark)	7.75	1.428	1	4.516	24.66	0.9474	93,300
TNTAs (light)	11.8	1103	0.9587	1.428	3.859	0.9486	5132
g-C_3N_4/TNTAs (dark)	13.21	829.3	0.8474	1.569	30.16	0.9482	29,290
g-C_3N_4/TNTAs (light)	13.43	65.86	1	0.9062	4.037	0.9289	2482

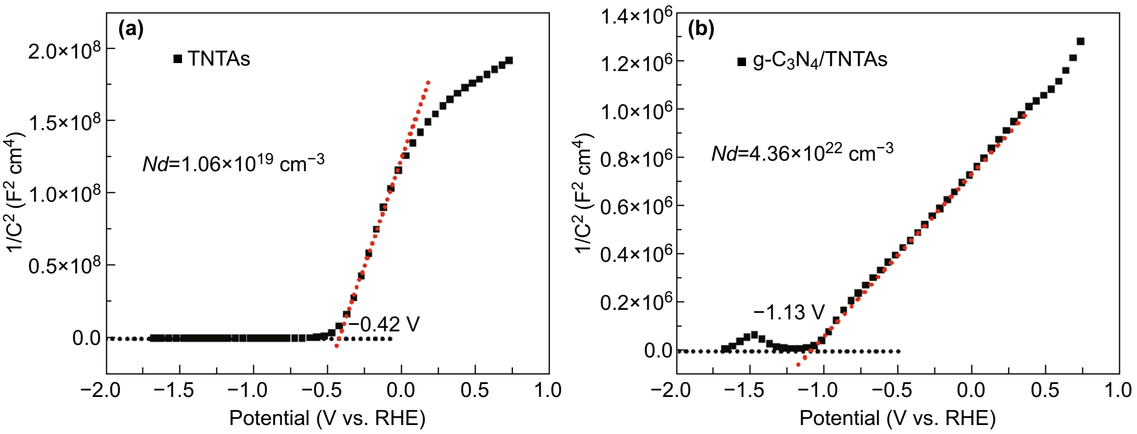

Fig. 10 Mott–Schottky images of **a** pristine TNTAs and **b** g-C_3N_4/TNTAs

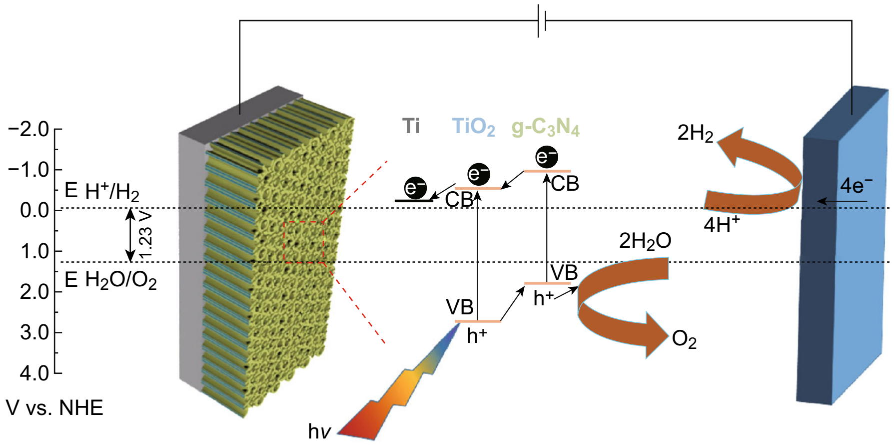

Fig. 11 Schematic diagram of the charge transfer mechanism of the g-C_3N_4/TNTA heterojunction electrode

of pristine TNTAs in Fig. 9a, indicating significantly higher charge carrier densities. The calculated charge carrier densities (N_d) for pristine TNTAs and g-C_3N_4/TNTAs were 1.06×10^{19} and 4.36×10^{22} cm^{-3}, respectively. Based on these values, it was inferred that the junction supplied more charge carrier density upon addition of g-C_3N_4. As current density is directly related to charge carrier density in a semiconductor photoanode, the calculated carrier density values strongly indicate that the enhanced PEC properties of the g-C_3N_4/TNTAs were a result of the increased availability of free charge carriers within the donor states of the system, which is in agreement with the PEC efficiencies (Fig. 7a, c). Overall, these conclusions can be attributed to the presence of g-C_3N_4 layers that promote the charge carrier separation. Moreover, the flat band potentials (E_{fb}) of the samples were estimated by extrapolating their linear fits to $1/C^2 = 0$. According to the MS results, the conduction bands (CB) of pristine TNTAs and g-C_3N_4/TNTAs were estimated at − 0.42 and − 1.13 V versus NHE, respectively. As is well-known, the CB potential of n-type semiconductors lies close to the E_{fb}. Therefore, the CB edges of pristine TNTAs and g-C_3N_4/TNTAs were at − 0.42 and − 1.13 V versus RHE, respectively.

On the basis of the aforementioned results, a possible mechanism for the improvement in PEC activity over g-C_3N_4/TNTAs was proposed (Fig. 11). In this mechanism, a well-matched heterojunction is formed by the combination of g-C_3N_4 and TNTAs because the valence and conduction bands of g-C_3N_4 are higher than those of TiO_2. Upon light irradiation, the electrons are excited from the valence band (VB) of g-C_3N_4 to its CB, which are then transferred to the CB of TiO_2 nanotubes and leave holes in the VB of g-C_3N_4 [38, 54]. Finally, electrons are transported to the counter electrode through the external circuit to be consumed by H^+ for the generation of H_2. The direction of charge migration is in accordance with the results of Mott–Schottky and OCP measurements. In addition, the holes generated in the VB of TiO_2 nanotubes are transferred to the VB of g-C_3N_4, and participate in the oxidation of water molecules. Thus, it has been established that the significant enhancement in photocurrent can be attributed to the construction of the g-C_3N_4/TNTAs heterojunction, which accelerates the migration of carriers and significantly suppresses the recombination of photogenerated electron–hole carriers.

4 Conclusions

In summary, an efficient, easy, and universal method was used to prepare the g-C_3N_4/TNTAs heterojunction with a g-C_3N_4 shell and TiO_2 nanotube array core, by powder coating with the cyanuric acid melamine supramolecular complex. The prepared g-C_3N_4/TNTAs exhibited an expanded optical absorption range and enhanced PEC activity. Moreover, the creation of a heterojunction of g-C_3N_4 and TNTAs significantly accelerated the migration of the charge carriers and greatly suppressed the recombination of the photogenerated electron–hole pairs. These results provide a deeper understanding of the role of semiconductor photoanodes during the PEC process of converting water to environmentally friendly hydrogen fuel.

Acknowledgements The authors greatly acknowledge financial support from the National Natural Science Foundation of China (Nos. 51702025, 51574047), Natural Science Foundation of Jiangsu Province (Nos. BK20160277, BK20150259).

References

1. M. Grätzel, Photoelectrochemical cells. Nature **414**, 338–344 (2001). https://doi.org/10.1038/35104607
2. F.E. Osterloh, Inorganic nanostructures for photoelectrochemical and photocatalytic water splitting. Chem. Soc. Rev. **42**, 2294–2320 (2013). https://doi.org/10.1039/C2CS35266D
3. G. Wang, H. Wang, Y. Ling, Y. Tang, X. Yang, R.C. Fitzmorris, C. Wang, J.Z. Zhang, Y. Li, Hydrogen-treated TiO_2 nanowire arrays for photoelectrochemical water splitting. Nano Lett. **11**(7), 3026–3033 (2011). https://doi.org/10.1021/nl201766h
4. Y. Hou, F. Zuo, A. Dagg, P. Feng, A three-dimensional branched cobalt-doped α-Fe_2O_3 Nanorod/$MgFe_2O_4$ heterojunction array as a flexible photoanode for efficient photoelectrochemical water oxidation. Angew. Chem. Int. Ed. **125**(4), 1286–1290 (2013). https://doi.org/10.1002/ange.201207578
5. K.D. Malviya, D. Klotz, H.D. Dmitry, D. Shlenkevich, A. Tsyanok, H. Mor, A. Rothschild, Influence of Ti doping levels on the photoelectrochemical properties of thin-film hematite (α-Fe_2O_3) photoanodes. J. Phys. Chem. C **121**(8), 4206–4213 (2017). https://doi.org/10.1021/acs.jpcc.7b00442
6. F.X. Xiao, J. Miao, B. Liu, Layer-by-layer self-assembly of CdS quantum dots/graphene nanosheets hybrid films for photoelectrochemical and photocatalytic applications. J. Am. Chem. Soc. **136**(4), 1559–1569 (2014). https://doi.org/10.1021/ja411651e
7. X. Wang, C. Liow, D. Qi, B. Zhu, W.R. Leow, H. Wang, C. Xue, X. Chen, S. Li, Programmable photo-electrochemical hydrogen evolution based on multi-segmented CdS-Au nanorod arrays. Adv. Mater. **26**(21), 3506–3512 (2014). https://doi.org/10.1002/adma.201306201
8. C.H. Liu, Y.Y. Qiu, F. Wang, L. Li, Q. Liang, Z.D. Chen, Electrodeposition of ZnO nanoflake-based photoanode sensitized by carbon quantum dots for photoelectrochemical water oxidation. Ceram. Int. **43**(6), 5329–5333 (2017). https://doi.org/10.1016/j.ceramint.2016.11.129
9. M. Shao, F. Ning, M. Wei, D.G. Evans, X. Duan, Hierarchical nanowire arrays based on ZnO core-layered double hydroxide shell for largely enhanced photoelectrochemical water splitting. Adv. Fun. Mater. **24**(5), 580–586 (2014). https://doi.org/10.1002/adfm.201301889
10. M. Li, R. Zhao, Y. Su, J. Hu, Z. Yang, Y. Zhang, Synthesis of $CuInS_2$ nanowire arrays via solution transformation of Cu_2S self-template for enhanced photoelectrochemical performance. Appl. Catal. B **203**, 715–724 (2017). https://doi.org/10.1016/j.apcatb.2016.10.051
11. W. Shi, X. Zhang, J. Brillet, D. Huang, M. Li, M. Wang, Y. Shen, Significant enhancement of the photoelectrochemical activity of WO_3 nanoflakes by carbon quantum dots decoration. Carbon **105**, 387–393 (2016). https://doi.org/10.1016/j.carbon.2016.04.051
12. Y.C. Pu, G. Wang, K.D. Chang, Y. Ling, Y.K. Lin et al., Au nanostructure-decorated TiO_2 nanowires exhibiting photoactivity across entire UV-visible region for photoelectrochemical water splitting. Nano Lett. **13**(8), 3817–3823 (2013). https://doi.org/10.1021/nl4018385
13. X.P. Chen, Z.X. Zhang, L.N. Chi, A.K. Nair, W.F. Shangguang, Z. Jiang, Recent advances in visible-light-driven photoelectrochemical water splitting: catalyst nanostructures and reaction systems. Nano Micro Lett. **8**(1), 1–12 (2016). https://doi.org/10.1007/s40820-015-0063-3
14. D.D. Qin, Y.P. Bi, X.J. Feng, W. Wang, G.D. Barber, T. Wang, Y.M. Song, X.Q. Lu, T.E. Mallouk, Hydrothermal growth and photoelectrochemistry of highly oriented, crystalline anatase TiO_2 nanorods on transparent conducting electrodes. Chem. Mater. **27**(12), 4180–4183 (2015). https://doi.org/10.1021/acs.chemmater.5b00782
15. X. Li, J. Li, J. Bai, Y. Dong, L. Li, B. Zhou, The inhibition effect of tert-butyl alcohol on the TiO_2 nano arrays photoelectrocatalytic degradation of different organics and its mechanism. Nano Micro Lett. **8**(3), 221–231 (2016). https://doi.org/10.1007/s40820-015-0080-2
16. H. Wu, D.D. Li, X.F. Zhu, C.Y. Yang, D.F. Liu, X.Y. Chen, Y. Song, L.F. Lu, High-performance and renewable supercapacitors based on TiO_2 nanotube array electrodes treated by an electrochemical doping approach. Electrochim. Acta **116**, 129–136 (2014). https://doi.org/10.1016/j.electacta.2013.10.092
17. S.Y. Zhang, D.L. Yu, D.D. Li, Y. Song, J.F. Che, S.Y. You, X.F. Zhu, Forming process of anodic TiO_2 nanotubes under a preformed compact surface layer. J. Electrochem. Soc. **161**(10), E135–E141 (2014). https://doi.org/10.1149/2.0661410jes
18. R. Reichert, Z. Jusys, R.J. Behm, Au/TiO_2 Photo (electro) catalysis: the role of the Au cocatalyst in photoelectrochemical water splitting and photocatalytic H_2 evolution. J. Phys. Chem. C **119**(44), 24750–24759 (2015). https://doi.org/10.1021/acs.jpcc.5b08428

19. X. Wang, J. Zhao, Y. Kang, L. Li, X. Xu, Photoelectrochemical properties of Fe-doped TiO_2 nanotube arrays fabricated by anodization. J. Appl. Electrochem. **44**(1), 1–4 (2014). https://doi.org/10.1007/s10800-013-0617-3
20. J. Song, M. Zheng, X. Yuan, Q. Li, F. Wang et al., Electrochemically induced Ti^{3+} self-doping of TiO_2 nanotube arrays for improved photoelectrochemical water splitting. J. Mater. Sci. **52**(12), 6976–6986 (2017). https://doi.org/10.1007/s10800-013-0617-3
21. P. Wang, J. Wang, T. Ming, X. Wang, H. Yu, J. Yu, Y. Wang, M. Lei, Dye-sensitization-induced visible-light reduction of graphene oxide for the enhanced TiO_2 photocatalytic performance. ACS Appl. Mater. Interfaces **5**(8), 2924–2929 (2013). https://doi.org/10.1021/am4008566
22. M. Krbal, H. Sopha, V. Podzemna, S. Das, J. Prikryl, J.M. Macak, TiO_2 nanotube/chalcogenide-based photoelectrochemical cell: nanotube diameter dependence study. J. Phys. Chem. C **121**(11), 6065–6071 (2017). https://doi.org/10.1021/acs.jpcc.6b11283
23. W. Yang, Y. Yu, M.B. Starr, X. Yin, Z. Li, A. Kvit, S. Wang, P. Zhao, X.D. Wang, Ferroelectric polarization-enhanced photoelectrochemical water splitting in TiO_2-$BaTiO_3$ core-shell nanowire photoanodes. Nano Lett. **15**(11), 7574–7580 (2015). https://doi.org/10.1021/acs.nanolett.5b03988
24. Q. Liu, H. Lu, Z. Shi, F. Wu, J. Guo, K. Deng, L. Li, 2D $ZnIn_2S_4$ nanosheet/1D TiO_2 nanorod heterostructure arrays for improved photoelectrochemical water splitting. ACS Appl. Mater. Interfaces **6**(19), 17200–17207 (2014). https://doi.org/10.1021/am505015j
25. Y.C. Bao, K.Z. Chen, AgCl/Ag/g-C_3N_4 hybrid composites: preparation, visible light drived photocatalytic activity and mechanism. Nano Micro Lett. **8**(2), 182–192 (2016). https://doi.org/10.1007/s40820-015-0076-y
26. Q. Xu, B. Cheng, J. Yu, G. Liu, Making co-condensed amorphous carbon/g-C_3N_4 composites with improved visible-light photocatalytic H_2-production performance using Pt as cocatalyst. Carbon **118**, 241–249 (2017). https://doi.org/10.1016/j.carbon.2017.03.052
27. Q. Liang, J. Jin, M. Zhang, C.H. Liu, S. Xu, C. Yao, Z. Li, Construction of mesoporous carbon nitride/binary metal sulfide heterojunction photocatalysts for enhanced degradation of pollution under visible light. Appl. Catal. B **218**(5), 545–554 (2017). https://doi.org/10.1016/j.apcatb.2017.07.003
28. Y. Hou, Z. Wen, S. Cui, X. Guo, J. Chen, Constructing 2D porous graphitic C_3N_4 nanosheets/nitrogen-doped graphene/layered MoS_2 ternary nanojunction with enhanced photoelectrochemical activity. Adv. Mater. **25**(43), 6291–6297 (2013). https://doi.org/10.1002/adma.201303116
29. Y. Tian, B. Chang, J. Lu, J. Fu, F. Xi, X. Dong, Hydrothermal synthesis of graphitic carbon nitride-Bi_2WO_6 heterojunctions with enhanced visible light photocatalytic activities. ACS Appl. Mater. Interfaces **5**(15), 7079–7085 (2013). https://doi.org/10.1021/am4013819
30. M. Shalom, S. Gimenez, F. Schipper, I. Herraiz-Cardona, J. Bisquert, M. Antonietti, Controlled carbon nitride growth on surfaces for hydrogen evolution electrodes. Angew. Chem. Int. Ed. **53**(14), 3654–3658 (2014). https://doi.org/10.1002/ange.201309415
31. H. Song, K. Jo, B.Y. Jung, G.Y. Jung, Fabrication of periodically aligned vertical single-crystalline anatase TiO_2 nanotubes with perfect hexagonal open-ends using chemical capping materials. Nano Res. **7**(1), 104–109 (2014). https://doi.org/10.1007/s12274-013-0377-8
32. M. Xiong, L. Chen, Q. Yuan, J. He, S.L. Luo, C.T. Au et al., Controlled synthesis of graphitic carbon nitride/beta bismuth oxide composite and its high visible-light photocatalytic activity. Carbon **86**, 217–224 (2015). https://doi.org/10.1016/j.carbon.2015.01.023
33. R. Lei, J. Jian, Z. Zhang, B. Song, R. Wu, Bifunctional Ag/$C_3N_{4.5}$ composite nanobelts for photocatalysis and antibacterium. Nanotechnology **27**, 395603 (2016). https://doi.org/10.1088/0957-4484/27/39/395603
34. G.X. Wang, X.P. Shen, J. Yao, J. Park, Graphene nanosheets for enhanced lithium storage in lithium ion batteries. Carbon **47**(8), 2049–2053 (2009). https://doi.org/10.1016/j.carbon.2009.03.053
35. M. Li, R. Zhao, Y. Su, J. Hu, Z. Yang, Y. Zhang, Hierarchically $CuInS_2$ Nanosheet-constructed nanowire arrays for photoelectrochemical water splitting. Adv. Mater. Interfaces **3**(20), 1600494 (2016). https://doi.org/10.1002/admi.201600494
36. J. Wang, Z.Q. Lin, Freestanding TiO_2 nanotube arrays with ultrahigh aspect ratio via electrochemical anodization. Chem. Mater. **20**(4), 1257–1261 (2008). https://doi.org/10.1021/cm7028917
37. T. Ohsaka, F. Izumi, Y. Fujiki, Raman spectrum of anatase, TiO_2. J. Raman Spectrosc. **7**(6), 321–324 (1978). https://doi.org/10.1002/jrs.1250070606
38. H. Liu, D. Chen, Z. Wang, H. Jing, R. Zhang, Microwave-assisted molten-salt rapid synthesis of isotype triazine-/heptazine based g-C_3N_4 heterojunctions with highly enhanced photocatalytic hydrogen evolution performance. Appl. Catal. B **203**, 300–313 (2017). https://doi.org/10.1016/j.apcatb.2016.10.014
39. D.J. Martin, K. Qiu, S.A. Shevlin, A.D. Handoko, X. Chen, Z. Guo, J. Tang, Highly efficient photocatalytic H_2 evolution from water using visible light and structure-controlled graphitic carbon nitride. Angew. Chem. Int. Ed. **126**(35), 9394–9399 (2014). https://doi.org/10.1002/anie.201403375
40. S. Hu, L. Ma, J. You, F. Li, Z. Fan, G. Lu, D. Liu, J. Gui, Enhanced visible light photocatalytic performance of g-C_3N_4 photocatalysts co-doped with iron and phosphorus. Appl. Surf. Sci. **311**, 164–171 (2014). https://doi.org/10.1016/j.apsusc.2014.05.036
41. Q.H. Liang, Z. Li, X.L. Yu, Z.H. Huang, F.Y. Kang, Q.H. Yang, Macroscopic 3D porous graphitic carbon nitride monolith for enhanced photocatalytic hydrogen evolution. Adv. Mater. **27**(31), 4634–4639 (2015). https://doi.org/10.1002/adma.201502057
42. Z.F. Jiang, C.Z. Zhu, W.M. Wan, K. Qian, J.M. Xie, Constructing graphite-like carbon nitride modified hierarchical yolk-shell TiO_2 spheres for water pollution treatment and hydrogen production. J. Mater. Chem. A **4**(5), 1806–1818 (2016). https://doi.org/10.1039/C5TA09919F
43. J. Xu, Y. Li, X. Zhou, Y. Li, Z.D. Gao, Y.Y. Song, P. Schmuki, Graphitic C_3N_4-sensitized TiO_2 nanotube layers: a visible-light activated efficient metal-free antimicrobial platform. Chem. Eur. J. **22**(12), 3947–3951 (2016). https://doi.org/10.1002/chem.201505173
44. C. Zhao, G. Tan, J. Huang, W. Yang, H. Ren, A. Xia, Preparation of self-assembled spherical g-C_3N_4/tz-$Bi_{0.92}Gd_{0.08}VO_4$ heterojunctions and their mineralization properties. ACS Appl. Mater. Interfaces **7**(43), 23949–23957 (2015). https://doi.org/10.1021/acsami.5b06501
45. Q. Liang, M. Zhang, C. Liu, S. Xu, Z. Li, Sulfur-doped graphitic carbon nitride decorated with zinc phthalocyanines towards highly stable and efficient photocatalysis. Appl. Catal. A **519**(5), 107–115 (2016). https://doi.org/10.1016/j.apcata.2016.03.033
46. C.H. Liu, Y.Y. Qiu, F. Wang, K. Wang, Q. Liang, C.Z. Chen, Design of core–shell-structured ZnO/ZnS hybridized with graphite-like C_3N_4 for highly efficient photoelectrochemical water splitting. Adv. Mater. Interfaces **4**(21), 1700681 (2017). https://doi.org/10.1002/admi.201700681
47. S.B.A. Hamid, S.J. The, C.W. Lai, S. Perathoner, G. Centi, Applied bias photon-to-current conversion efficiency of ZnO enhanced by hybridization with reduced graphene oxide.

J. Energy Chem. **26**(2), 302–308 (2017). https://doi.org/10.1016/j.jechem.2016.11.006

48. T. An, J. Tang, Y. Zhang, Y. Quan, X. Gong, A.M. Al-Enizi, A.A. Elzatahry, L. Zhang, G.F. Zheng, Photoelectrochemical conversion from graphitic C_3N_4 quantum dot decorated semiconductor nanowires. ACS Appl. Mater. Interfaces **8**(20), 12772–12779 (2016). https://doi.org/10.1021/acsami.6b01534
49. H.J. Yun, H. Lee, N.D. Kim, J. Yi, Characterization of photocatalytic performance of silver deposited TiO_2 nanorods. Electrochem. Commun. **11**(2), 363–366 (2009). https://doi.org/10.1016/j.elecom.2008.11.044
50. L. Ye, D. Wang, S. Chen, Fabrication and enhanced photoelectrochemical performance of MoS_2/S-doped g-C_3N_4 heterojunction film. ACS Appl. Mater. Interfaces **8**(8), 5280–5289 (2016). https://doi.org/10.1021/acsami.5b11326
51. B. Liu, X.B. Li, Y.J. Gao, Z.J. Li, Q.Y. Meng, C.H. Tung, L.Z. Wu, A solution-processed, mercaptoacetic acid-engineered CdSe quantum dot photocathode for efficient hydrogen production under visible light irradiation. Energy Environ. Sci. **8**(5), 1443–1449 (2015). https://doi.org/10.1039/C5EE00331H
52. Y.C. Wang, Y.Y. Zhang, J. Tang, H.J. Wu, M. Xu, Z. Peng, X.G. Gong, G. Zheng, Simultaneous etching and doping of TiO_2 nanowire arrays for enhanced photoelectrochemical performance. ACS Nano **7**(10), 9375–9383 (2013). https://doi.org/10.1021/nn4040876
53. J. Resasco, H. Zhang, N. Kornienko, N. Becknell, H. Lee, J.H. Guo, A.L. Briseno, P.D. Yang, TiO_2/$BiVO_4$ nanowire heterostructure photoanodes based on type II band alignment. ACS Cent. Sci. **2**(2), 80–88 (2016). https://doi.org/10.1021/acscentsci.5b00402
54. K. Sridharan, E. Jang, T.J. Park, Novel visible light active graphitic C_3N_4–TiO_2 composite photocatalyst: synergistic synthesis, growth and photocatalytic treatment of hazardous pollutants. Appl. Catal. B **142–143**, 718–728 (2013). https://doi.org/10.1016/j.apcatb.2013.05.077